Available online at www.sciencedirect.com
ScienceDirect
Trans. Nonferrous Met. Soc. China 35(2025) 1937−1955
Transactions of Nonferrous Metals Society of China
www.tnmsc.cn

Corrosion behavior and performance degradation of aluminum−copper cable joints with magnetic pulse crimping in salt spray environment

Yuan-heng YAO[1], Shao-luo WANG[1], Hao JIANG[1], Jun-jia CUI[1,2], Guang-yao LI[1,2], Kai-dong LUO[3], Ling-hua XIA[3]

1. State Key Laboratory of Advanced Design and Manufacturing Technology for Vehicle, Hunan University, Changsha 410082, China;
2. Shenzhen Automotive Research Institute, Beijing Institute of Technology, Shenzhen 518118, China;
3. The First Product Department, FinDreoms Battery Co., Ltd., Huizhou 516083, China;

Received 20 September 2023; accepted 3 June 2024

Abstract: The corrosion resistance of aluminum (Al) cable−copper (Cu) terminal joints fabricated by magnetic pulse crimping (MPC) and hydraulic clamp crimping (HCC) was compared. Performance degradation was evaluated by mechanical and electrical properties. Additionally, corrosion behavior was analyzed by electrochemical testing. Microscopic characterization was performed by scanning electron microscopy (SEM) and energy dispersive spectroscopy (EDS). Results show that the tensile strength of the corroded joints is reduced. However, due to the advantages of high-speed forming and contact tightness unique to MPC, the contact resistance of the corroded joints still maintains excellent. Electrochemical tests demonstrate that the MPC joints have higher corrosion potentials and smaller corrosion currents, providing better corrosion resistance. The formation of a primary battery between Al and Cu at the lap joint leads to the formation of severer corrosion pits.

Key words: magnetic pulse crimping; aluminum−copper cable joint; salt spray corrosion; performance degradation; corrosion mechanism

1 Introduction

With environmental protection emerging as a global consensus, renewable electricity is gradually displacing fossil fuels. [1]. Meanwhile, cables, as a major tool for electricity transportation, have become the focus of the attention of researchers [2−4]. The use of aluminum (Al) in place of copper (Cu) for wires and cables is becoming an industry mainstream trend [5,6]. This is caused by the increasing price of Cu and the lightweight and excellent electrical conductivity of Al [7−9]. However, the application of Al instead of Cu cable involves the challenge of joining dissimilar materials. Fusing techniques such as laser beam welding tend to produce brittle intermetallic compounds (IMC) in welded joints, which could make it difficult to ensure strength and electrical conductivity [10]. For purely mechanical connection methods such as bolting, the clamping force needs to be considered to prevent failures from loosening [11]. Consequently, achieving a low-resistance, high-strength, and highly reliable connection between Al cables and Cu terminals remains an urgent challenge.

Magnetic pulse crimping (MPC) is an emerging joining process developed from electromagnetic pulse technology (EMPT) [12]. Lorenz force generated by electromagnetic induction is used to drive the outer tube to deform at high speed, which results in a locked structure.

Corresponding author: Shao-luo WANG, Tel: +86-731-88821445, E-mail: wsl0809@hnu.edu.cn
https://doi.org/10.1016/S1003-6326(25)66792-6

The impact velocity of MPC is huge and hardly generates additional heat [13]. The high-velocity impact can break the impurities and oxidation layers on the metal surface, thus greatly reducing the contact resistance of the two metals [14]. Hence, it has unique advantages in power transportation. Additionally, MPC is a highly efficient, green production, low energy consumption, and easily automated process [15].

In-depth investigations on process parameters and connection structures have been carried out by many scholars due to the multiple advantages of MPC. WEDDELING et al [16] designed joints with different structures and performed strength prediction. This allowed the light weight of the frame structure while maintaining high strength. LAI et al [17] performed quality inspection using vision for MPC joints of dissimilar materials. The images were processed using the Steger algorithm. Moreover, a neural network was successfully used to establish the relationship between contour and quality. KUMAR et al [18] added adhesive to MPC for the joint. The results showed that the addition of adhesive enhanced joint strength and air tightness. The crimping of Al−Cu wires employing magnetic pulses was achieved by RAJAK and KORE [19]. It had also been demonstrated that the joints under this process were more uniform, less resistive, and stronger than conventional crimped joints. KUMAR et al [20] developed a finite element model for analyzing the deformation and strength pattern of copper−steel electromagnetic crimped joints during the joining process. The accuracy was also verified using mechanical properties experiments of joints with different structures.

Whereas, most of the current research was conducted on the process and structure. The corrosion resistance of the joint is equally important in the application. Especially for dissimilar material joints prone to stress corrosion problems because their microstructure and chemical composition are very different [21,22]. The stress corrosion of SA508-309L welded joints was studied by DING et al [23]. Furthermore, the joints were treated by a pulsed current to eliminate the spinodal decomposition and *G*-phase, which resulted in aging resistance of the joints. YE et al [24] investigated the corrosion resistance of Al−Cu-brazed joints and slowed down the development of stress corrosion by adding Si. JANDAGHI et al [25] examined the corrosion behavior and microscopic characterization of explosion-welded Al−Cu dissimilar material joints. The effects of corrosion potential and concentration gradient on corrosion resistance were revealed. SAFARALI et al [26] investigated the effect of post-weld heat treatment on the corrosion performance of explosion welded interfaces of dissimilar material tubes. Additionally, dissimilar metals are also susceptible to galvanic corrosion due to the existence of electrode potential differences [27,28]. Concerning the study of joint corrosion aspects of EMPT, WANG et al [29] reported the corrosion performance of galvanized steel and Al welded joints to reveal the corrosion failure mechanism. The corrosion behavior of welding joints with Al−Fe was studied in a neutral salt spray environment by GENG et al [30]. The flat weld area was found to be galvanic corrosion. In contrast, the corrosion on the shear wave was mainly stress corrosion. However, the Al−Cu cable joints under the MPC process have significant variability in the connection form and microstructure from the above investigations. Hence, it is necessary to investigate the corrosion behavior and failure mechanism of Al−Cu cable joints under the MPC process.

In the present study, the corrosion resistance of Al−Cu cable connection joints under different processes was investigated. The MPC joints under different process parameters and hydraulic clamp crimping (HCC) joints were tested in neutral salt spray corrosion tests. The corrosion behavior and performance degradation laws of MPC and HCC joints were investigated in comparison. The mechanism of corrosion pit formation inside and outside of the lap zone and the mechanism of corrosion product stripping and shedding were revealed.

2 Experimental

2.1 Materials

Class A small-head DT70 Cu terminals according to GB/T 14315—2008 and three oxygen-free pure Al cables with cross-sectional areas of 50, 70 and 95 mm^2 (according to GB/T 12706.1—2020) were used. [31]. The outer diameter of its connection area is 15 mm and the inner diameter is 12 mm. The Al cable is made of oxygen-free pure

Al. It has advantages of lightweight, good electrical and thermal conductivity, good corrosion resistance, and low price. The diameters of the Al cables are 11.2, 9.8 and 8.0 mm, respectively. The diameter of the Cu terminal is 12 mm, which means that the crimp air gaps are 0.4, 1.1 and 2.0 mm, respectively. The cable was stripped to a length of 200 mm and inserted 41 mm into the terminal. The geometry and connection form of the cable joint specimen are shown in Fig. 1. The main performance parameters of pure Al and T2 purple Cu are shown in Table 1.

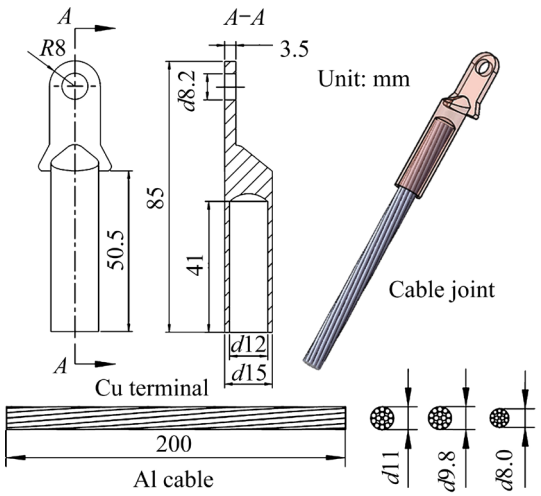

Fig. 1 Geometry and connection form of cable joint specimen

Table 1 Main performance parameters of pure Al and T2 purple Cu

Material	Density/ ($g \cdot cm^{-3}$)	Yield strength/ MPa	Tensile strength/ MPa	Young's modulus/ GPa
Al	2.7	55	136	70
T2 Cu	8.9	90	300	110

2.2 Joining process

Al cables and Cu terminals were connected by two connection processes to compare their performance. The MPC process to join the Al cable and Cu terminal is shown in Fig. 2(a). The magnetic pulse generator generates a high-frequency pulse current and flows through the coil during the MPC process. The pulse current is induced in the field shaper at this time. The outer tube (Cu terminal) located inside the field shaper also generates an induced current. Cu terminal moves in the opposite direction of the field shaper by electromagnetic force and hits the inner tube (Al cable) at high velocity. As a result, mechanical locking (crimping) and even metallurgical bonding (welding) are achieved between the two metals. A double-turn coil of 500 mm × 500 mm × 40 mm with a distance of 10 mm between the two turns was used. The 150 mm-diameter hole in the center of the coil was set up for the field shaper. The outer diameter of the magnet collector is 146 mm, the inner diameter is 60 mm, and the thickness is 80 mm. The working area of the field shaper is 15.6 mm in diameter and 10 mm in width, and the structure is a detachable type of counter-opening. The discharge energy of 35 kJ was chosen to join three different sizes of Al−Cu cable joint based on the preliminary experiments. The subsequent joints are named as Type I, II, and III joints, respectively.

The HCC process was used as the control group. The schematic diagram of the HCC process is shown in Fig. 2(b). A matched hexagonal die deforms the terminal neck inward, compressing the cable for the connection. The matched dies were applied to the crimping process. The whole process of compression was uniform and slow. Fixed pressure-holding for 1 min to prevent the Cu terminal deformation area from rebounding after the die was closed. The joint with a crimp gap of 1.1 mm was selected for the study using the HCC process according to the national standard. This type of joint is subsequently referred to as Type IV joint.

2.3 Neutral salt spray corrosion test

The connected cable joints were placed in a salt spray machine (model Q-FOG CCT—1100) for a neutral salt spray corrosion test. The corrosion test conditions were set according to the ASTM B117 standard: 5 wt.% NaCl solution, pH 6.5−7.2, and the temperature 35 °C. The samples were placed on the shelf during the test and the joints were overhung. Seven corrosion cycles of 0, 5, 10, 15, 20, 30, and 40 d (corresponding to T0−T6, respectively) were set. Three samples were made for each cycle of different samples. The samples were cleaned, dried and stored under a vacuum with silicon dioxide for subsequent testing.

2.4 Electrochemical corrosion performance test

A three-electrode system was selected to investigate the corrosion behavior of metals. The

system consisted of a working electrode, where the electrochemical reaction occurred, a reference electrode to provide a stable reference potential, and a counter electrode to complete the circuit, as illustrated in Fig. 3(a). The working electrodes are MPC joints, HCC joints, Cu terminals and Al cables as shown in Fig. 3(b), and all of which were prepared by grinding and polishing. The inactive surfaces were encapsulated for protection. The counter electrode was made of platinum and the reference electrode was a saturated calomel electrode (SCE). A 3.5 wt.% NaCl solution was used for the electrolyte. Before testing, the electrodes were immersed in the electrolyte for approximately 15 min to stabilize the real-time potential. The tests consisted of open-circuit potential measurements at a scan rate of 2 mV/s with polarization curves in the potential range of −1.4 to −0.2 V (vs SCE).

2.5 Performance evaluation and microscopic observation

Specimens under different processes were evaluated by comparing both mechanical and electrical properties. Mechanical properties evaluated by quasi-static tensile testing. Tensile tests were performed on a microcomputer-controlled electronic universal testing machine (model SUNS UTM5605X). The tensile test conditions for all sample parts were at room temperature. The loading speed for tensile was set as 3 mm/min. Three repetitions of the same type of sample were performed. A clamping pad was added to the Cu terminal side to avoid additional

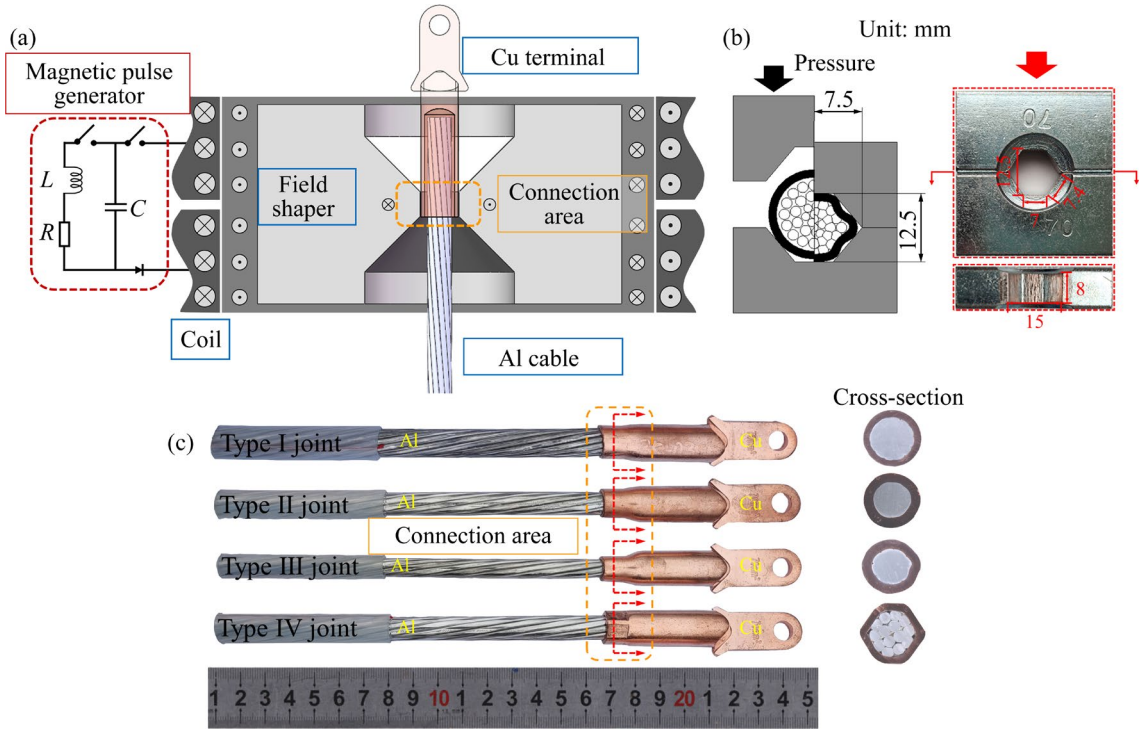

Fig. 2 Schematic diagram of cable joint connection: (a) MPC process; (b) HCC process; (c) Overall shape and cross-sectional view of four types of joints

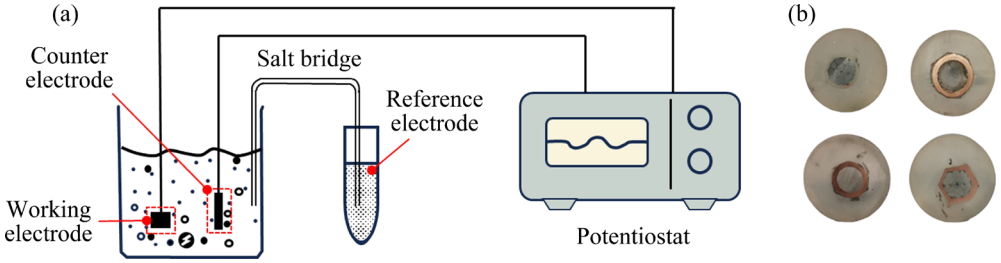

Fig. 3 Electrochemical performance testing: (a) Three-electrode system; (b) Working electrode sample

torque and slippage during test.

Microscopic observation of the sample was required for further study of the corrosion morphology and characterization of the microstructure and interfacial composition after corrosion. Typical portions of the sample were cut off after corrosion, ultrasonically cleaned with an ultrasonic cleaner and kept in a drying oven for 2 h. The processed specimens' surfaces and fractures were observed through an OLYMPUS 3D laser confocal microscope (model OLS5000), a scanning electron microscope (SEM, ZEISS Sigma HD) and energy dispersive spectroscopy (EDS), respectively. Moreover, a model SW−2000 resistance tester was applied to testing the electrical conductivity of joints in order to explore the difference in the electrical properties of joints. The distance between resistance test holders was fixed at 20 mm, with one clamped on the Al side at a distance of 5 mm from the Al−Cu junction. The other was held on the Cu side at a distance of 15 mm from the junction.

3 Results and discussion

3.1 Macroscopic corrosion behavior

The macroscopic morphology of all types of cable joints (I, II, III and IV) after corrosion under different cycles of salt spray environment is presented in Fig. 4. The left side shows the front view of different types of joints, and the right side shows the back view. The whole cable can be separated into three parts: the Cu terminal free end, the Al cable free end and the lap zone. It can be seen that the corrosion degree became more and more obvious with the increase of the corrosion cycle. The free end of the Al cable shows a distinct white oxide layer on the surface of the Al cable in the early stages of corrosion. This is due to the following reaction in the exposure of Al to air:

$$4Al+3O_2\rightarrow 2Al_2O_3 \quad (1)$$

This dense oxide layer will have a certain protective effect. However, the oxide layer on the Al surface begins to be eroded and peeled off after 10 d of corrosion. The oxide layer peels off most severely at 40 d. This is because the penetration of Cl^- from the salt solution into the oxide layer destroys the damaged Al wire matrix. The insoluble oxide becomes a soluble chloride. Al is reacted anodically in air in a salt spray environment as follows:

$$4Al\rightarrow 4Al^{3+}+12e \quad (2)$$

The most serious corrosion of the Al cable is observed at the lap joint with the Cu terminal. Severe corrosion pits appear in the later stages of corrosion. This is attributed to the formation of a Cu−Al primary battery at the contact site. Al is dissolved by losing electrons as the anode. Cu is protected by electrons as a cathode. Consequently, the dissolution of the Al cable is accelerated by the corrosive action of the primary battery. On the contrary, the Cu terminal does not corrode significantly under the protection of the primary battery. This can be demonstrated by the Al−Cu attachment site in the specimen shown in Fig. 4.

In the initial stage of corrosion, the free end of the unprotected Cu terminal is exposed to moist air to form a liquid film on the surface. Meanwhile, surface contaminants increase the conductivity of the liquid film to accelerate the electrochemical corrosion process. This promotes the production of Cu_2O, CuO and $Cu(OH)_2CO_2$ oxides on the surface. In summary, the patina produced by exposure to air is the product of reactions with substances such as O_2, CO_2 and H_2O. The main chemical reaction equations are as follows:

$$2Cu+O_2\rightarrow 2CuO \quad (3)$$

$$4Cu+O_2\rightarrow 2Cu_2O \quad (4)$$

$$2Cu+O_2+H_2O+CO_2\rightarrow Cu_2(OH)_2CO_2 \quad (5)$$

NaCl soluble salt particles are produced on the surface of Cu terminals exposed to salt spray as the corrosion cycle increases. The thin liquid coating of Cl^- is produced on the Cu terminals due to the effect of condensation. With the accumulation and continuous invasion of Cl^-, the Cu_2O oxide layer in the thin liquid film is broken and converted to CuCl or $CuCl_2^-$. Finally, the $Cu_2(OH)_3Cl$ is produced by the following reaction:

$$Cu^{2+}+H_2O+2OH^-+Cl^-\rightarrow Cu_2(OH)_3Cl \quad (6)$$

In addition, it is worth noting that the free end of the Cu terminal has a different degree of green patina on the front and back sides. From Fig. 4, it is obvious that the patina on the back side is distributed in an irregular area. This is due to the cable being placed face-up in the salt spray chamber. As a result, the droplets adsorbed on the terminals gather on the back side, and converge into liquid and eventually drip off. The flow of liquid prevents

Fig. 4 Macroscopic morphology of cable joints with different corrosion cycles on both sides: (a) Type I; (b) Type II; (c) Type III; (d) Type IV

the formation of patina. In addition, there are obvious traces of liquid flow on the backside.

A comparison of several types of cable joints indicated that the crimp is not tight due to the small air gap in Type I. This results in the salt spray being more likely to invade the joint along the gaps in the lap area and less likely to collect at the lap. Hence, the corrosion level at the lap edge is small and the corrosion pits are smaller, but the corrosion inside the joint is more serious. Type II joints are tighter because they have a more suitable air gap. As a result, the joint provides a good airtight seal and it is difficult for salt spray to enter the interior of the joint lap area for corrosion. The salt spray droplets accumulate on the back of the interface, where primary cell corrosion mainly occurs. Hence, the

more obvious corrosion pits appear on the lap area. Type III joint has excessive air gap and high collision velocity. Al cable is prone to over-shearing. In addition, the stress concentration in the deformation zone is great, which makes it easy for stress corrosion to occur causing large areas of pitting. Furthermore, there are also effects of galvanic corrosion. Thus, the corrosion at the lap edge is greater and the corrosion pits are larger. Type IV joints are less airtight owing to the numerous gaps at the interface. A large amount of salt spray enters the interior of the joint, causing severe oxidation and corrosion inside the joint. In terms of macroscopic appearance, therefore, the corrosion at the lap joint of the Type II joint is more serious. This also demonstrates the good tightness of the Type II joints.

3.2 Electrochemical corrosion behavior

In the electrochemical performance testing section, the study compares the corrosion resistance between HPC and HCC joints, specifically focusing on the more compact Type II and Type IV joints. The magnitude of the open circuit potential (OCP) reflects the thermodynamic parameters of these sites in the joint corrosion system. Comparing the OCP of different joint areas allows for an assessment of their respective corrosion tendencies. Higher OCP values at the welds indicate a lower tendency for corrosion, meaning that they are less likely to corrode under natural conditions. Conversely, more negative OCP suggests a higher susceptibility to corrosion.

Type II and Type IV joints were selected for comparison in the electrochemical performance testing to evaluate the corrosion resistance between MPC and HCC joints. Open-circuit potentials (OCPs) were measured at the centers of Al cables, Cu terminals, HCC, and MPC joints as illustrated in Fig. 5(a). These OCPs indicate thermo-dynamic parameters within the joint corrosion system and can be used to assess the corrosion tendencies of different joint locations. It is observed that the Cu terminals exhibit the highest OCP, while the Al cables show the lowest OCP. The OCPs of MPC joints are higher than those of the HCC joints, indicating a greater electronegativity in HCC joints relative to MPC joints. This electro-negativity predisposes the crimped areas of HCC joints to act preferentially as anodes in the corrosion system, leading to their higher susceptibility to corrosion.

Figure 5(b) presents the polarization curves of both types of joints. It is observed that the corrosion potential of Cu terminals, HCC joints, and MPC joints are all higher than that of the Al base material. The specific electrochemical corrosion parameters of the work are detailed in Table 2. Specifically, the MPC joints demonstrate a higher corrosion potential and lower corrosion current density compared to hydraulic joints, indicating superior corrosion resistance. This enhanced performance is attributed to the higher proportion of Al base material in the joints, resulting in a lower overall corrosion rate compared to the Cu base material.

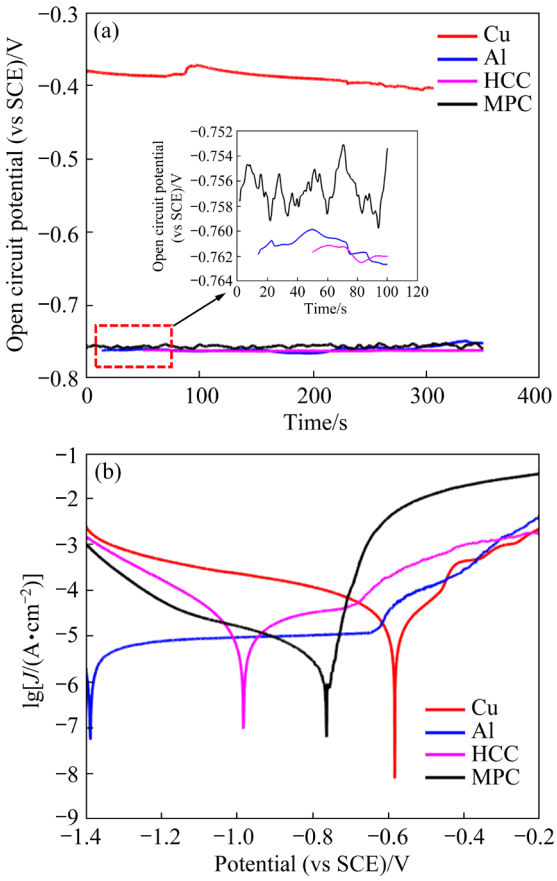

Fig. 5 Electrochemical corrosion results of joint: (a) Open circuit potential; (b) Polarization curves

Table 2 Electrochemical corrosion parameters for polarization curves

Joint	φ_{corr}(vs SCE)/V	J_{corr}/(10^{-6} A·cm^{-2})
Cu	−0.963	2.954
Al	−1.403	2.009
HCC	−0.963	6.394
MPC	−0.785	2.285

3.3 Performance degradation

The performance curves and failure samples of cable joints after different cycles of salt spray corrosion are shown in Fig. 6. The change in tensile strength of the Type I joint after corrosion is represented in Fig. 6(a). It is evident that the tensile load tends to increase and then decrease with the increasing cycles of corrosion. The tensile strength increases significantly during the first few corrosion cycles compared to the uncorroded specimen (T0 stage). However, it starts to decrease in the T3−T5 stage. Furthermore, it decreases rapidly in the T6 stage. The maximum decrease is 5.82%. This is because salt spray invades the inside of the terminals during the first few corrosion cycles. Salt particles attach between the cable and the terminal, which leads to increased friction at the lap joint, thus increasing the peak loads. The shear load on the Al cable decreases as corrosion increases. The failure sample also indicates that the later corrosion

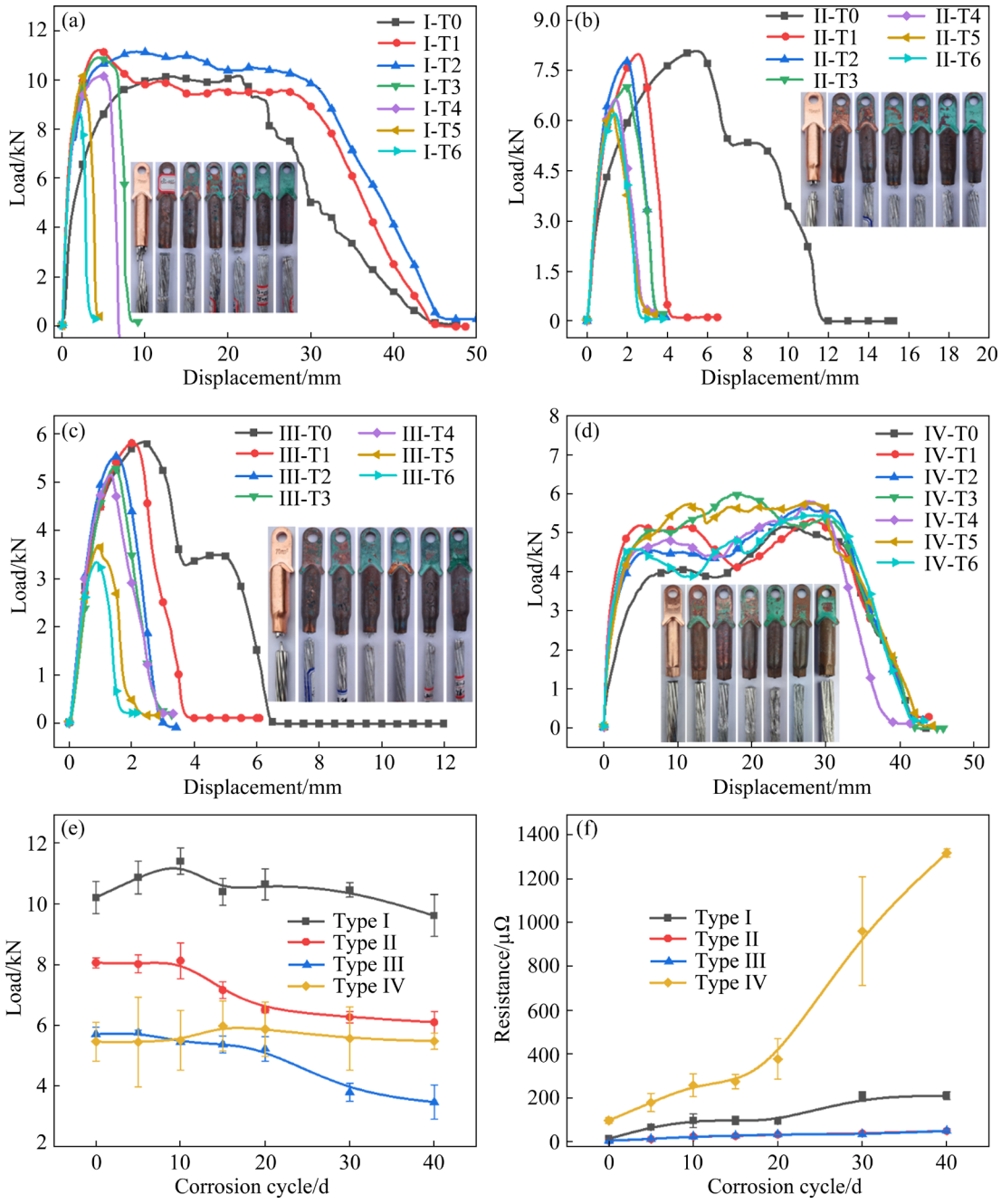

Fig. 6 Performance change curves of cable joints with different corrosion cycles: (a−d) Load−displacement curves of I−IV joints, respectively; (e) Comparison of tensile load after corrosion; (f) Comparison of electrical resistance after corrosion

samples are cable fractures. In terms of electrical properties, the electrical conductivity properties are reduced with increasing corrosion cycles. The salt spray invaded the cable easily since the Type I joints are not sufficiently compacted. As a result, the resistance increases rapidly in salt spray environments. The resistance of the uncorroded specimen is 14.0 μΩ. After 40 d of corrosion, the resistance of the specimen increases by 15 times to 210.2 μΩ.

There are sufficient air gaps in the Type II and III joints to make the joints crimp tightly. This results in the rapid corrosion of Al cables due to the action of the primary battery. As a result, the change in tensile load tends to decrease. Moreover, the failure mode is all cables fractured. After 40 d of corrosion, the load of the Type II joint is reduced from the initial 8.1 to 6.1 kN (a 24.34% reduction). However, the electrical performance of the Type II joint is reduced less compared to the Type I. It increases from the initial 5.2 to 49.8 μΩ, an increase of 9.6 times. Type III joints exhibit poor corrosion resistance due to a large air gap, which leads to over-shearing of the Al cable at the interface. After 40 d of corrosion, there is a 39.11% decrease in tensile load from 5.7 to 3.5 kN. The resistance increases from 5.6 to 49.6 μΩ.

After 20 d of corrosion of the Type IV joint, the failure mode changes from pull-off to cable fracture of the Al cable. This is due to severe erosion of the inner surface of the Al cable in the lap joint area. Besides, the electrical performance is severely degraded as the corrosion cycle increases. The change in tensile strength is more stable after 40 d of corrosion in a salt spray environment. However, the resistance rises from 97.2 to 1316.5 μΩ (a rise of approximately 14 times).

It is worth to note that the slopes of the tensile curves of the corroded joints are higher than those of the uncorroded specimens (see Figs. 6(a−d)). This is attributed to the presence of oxides and salt particles after corrosion, which increases the stiffness of the joints and makes the cable stiffness rise. Besides that, the non-lap zone of the cable joints exhibits different corrosion characteristics. The lap zone is protected by Cu due to the primary battery as mentioned above, and Al suffers severe corrosion. However, a dense oxide layer $Al(OH)_3$ is formed on the Al surface at the free end, which has some inhibition effect on corrosion. In contrast, Cu exposed to air is more susceptible to oxygen absorption corrosion. The formation of loose corrosion products on the surface accelerated the entry of H_2O and O_2, making Cu more susceptible to corrosion.

3.4 Corrosion pit depth

The ultra-depth microscope was used to profile two different processes (Types II and IV) of joints under the same specification in order to obtain an accurate picture of the shape and depth of corrosion pits on the Al cable. The generated 3D cloud image is shown in Fig. 7. The scanned Al cable exhibits surface noise on both sides due to the fact that its outer contour is a twisted and deformed cylinder. Therefore, this position should be avoided during data measurement.

From the corrosion morphology of the two joints, it can be found that the corrosion pits are deeper and deeper as the corrosion cycle is extended. Furthermore, the most obvious corrosion occurs at the location where Al and Cu converge. It is attributed to the galvanic corrosion reaction at this location. However, the corrosion pits of Type II joints are more pronounced than Type IV joints. The reason for this phenomenon is that Type II joints are better sealed. It is hard for the salt spray to enter the joint and it gathers at the junctions. As a result, it can provide good internal protection to the joint. On the contrary, the salt spray can easily enter the Type IV joints and erode the inside of the joints. Hence, the electrical performance decreases significantly after several corrosion cycles.

The deepest locations of corrosion pits at different corrosion cycles were selected for measurement and recorded by observing 3D scan cloud images. The corrosion cycle−corrosion pit depth variation curves are illustrated in Fig. 8. Since Type II joints have the tightest bonding, the Al and Cu of the joints are in close contact to form a primary battery, which results in rapid galvanic corrosion. As a result, Type II joints corrode faster at the beginning of the corrosion process than Type IV joints, which are not in close contact. The slope of the curve begins to decrease slowly in the later stages of corrosion. This is due to the large number of corrosion products generated at the interface that prevented Cl^- from entering the corrosion pit, which slowed down further erosion to some extent. In contrast, the corrosion pattern of Type IV joints

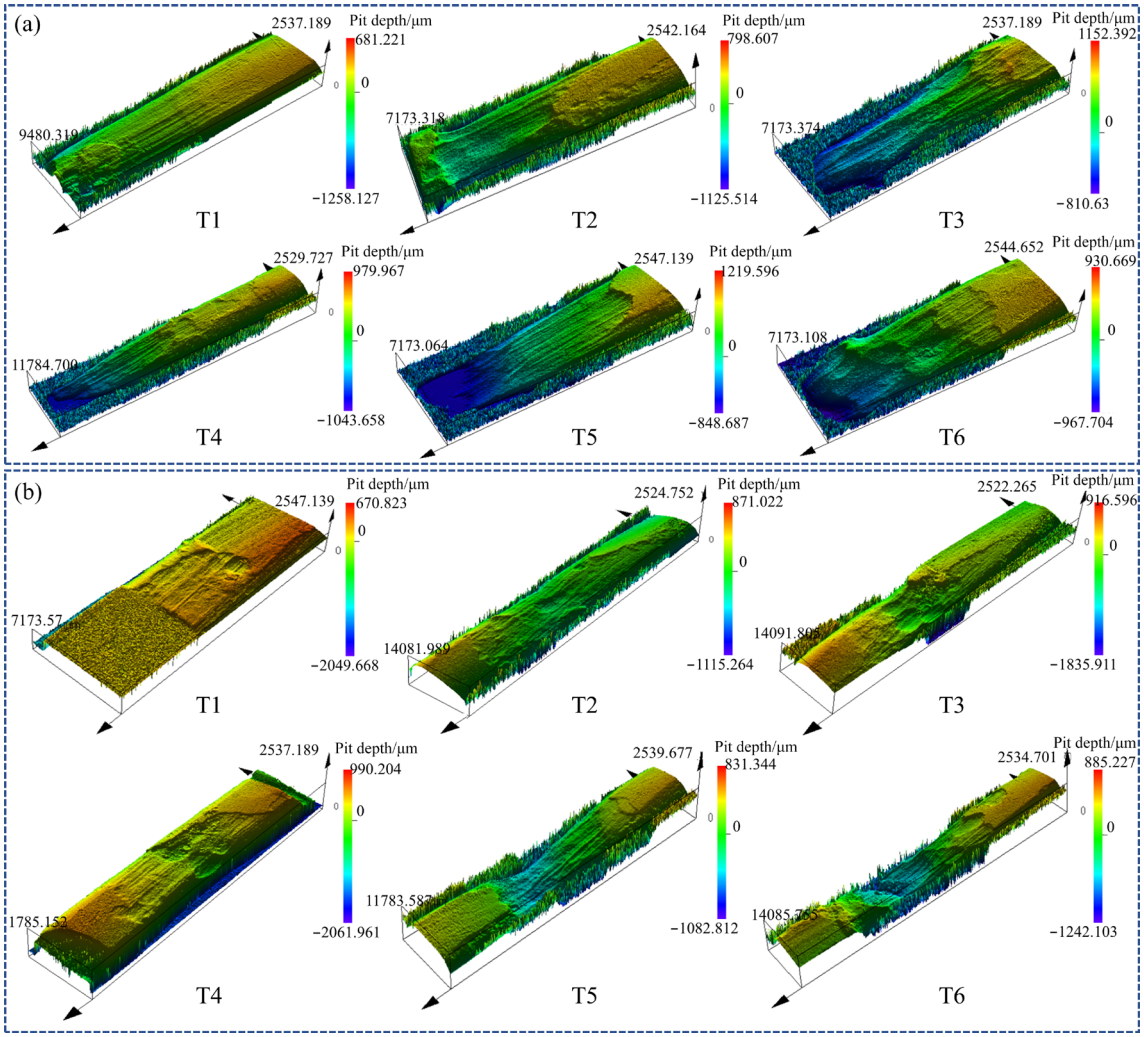

Fig. 7 3D cloud images of Al cable corrosion at interface of Al−Cu cable joint under different corrosion cycles: (a) Type II joints; (b) Type IV joints

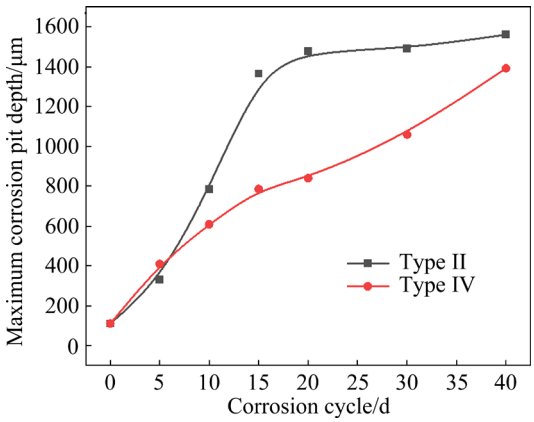

Fig. 8 Maximum corrosion pit depth on Al cable with variation of time

is linear. This is due to the fact that the joints are not tight enough, causing the salt spray to have difficulty collecting in the joints. The salt spray flows freely inside the terminal. Consequently, the Al cable is exposed to a relatively uniform salt spray attack. Additionally, it is found that after 40 d of corrosion, the maximum corrosion pit depth of Al cable reaches nearly 1600 μm. This indicates that the cable has almost failed (a single Al wire has a diameter of about 2000 μm). Therefore, it is necessary for engineering application and industrialization to obtain the evolution rules of corrosion pit depth and corrosion time, and thus to predict the service life.

3.5 Corrosion fracture

SEM and EDS analyses were performed to investigate the post-corrosion surface and fracture morphology, as well as corrosion products, of Al−Cu cable joints. Three typical locations were selected from the pull-off Type I joint for observation: the inner surface of the Cu terminal,

the outer surface of the Al cable and the corrosion pit of the Al cable. The observation position schematic diagram and surface morphology are shown in Fig. 9. It is notable that the positions of Figs. 9(a, c) correspond to each other. It can be seen in Fig. 9(a) that the pulled-off Al cable is attached to the smooth surface of the Cu surface. Observation of the Al layer reveals that the surface is covered with transverse and longitudinal microcracks as well as bright white corrosion products. This is due to the residual stresses caused by the peeling and corrosion of the Al cable during the tensile process, which leads to the generation of microcracks in all directions. While the Cu terminal is cathodically protected, the surface condition is well and no cracks are found. Figure 9(b) shows the morphology of corrosion pits at the lap joint. From the magnified view, it can be seen that the corrosion morphology is pitting tiny corrosion pits. This is the formation of Al cable corrosion products of pitting corrosion. Figure 9(c) presents the surface morphology of the pulled off Al cable. The rough surface is the fracture of the Al cable after stripping under tensile stress. A large number of microcracks and bright white oxides are also found. There are also plenty of scratches along the stress direction.

The SEM images of the tensile fractures of the Al cables with Type II and III joints after 10 d of corrosion are given in Fig. 10. It is observed that the inside of the Al cable also suffered from a certain degree of corrosion. This is mainly attributed to the existing gap between the core wires and the galvanic couple corrosion at the joint lap. The corrosion of the outer surface makes it easy for the salt spray droplets to penetrate inside and causes the corrosion of the inner core wire. The fracture morphology after corrosion appears with a large number of equiaxed dimples and shear dimples in the transient fracture region. It is noticed that stress cracking is present in the isometric dimples, as illustrated in Areas 1 and 3. Corrosion cracks are accelerated under tensile stress. The rate of initial corrosion microcrack expansion is accelerated. The fracture morphology of the lateral side of the Al core wire shows a dry riverbed-like appearance due to salt spray erosion between the wires as well. A large number of cracked fragments are found, as shown in Area 2. In addition, the shear dimples appear in the peripheral cables during the tensile process, as shown in Area 4.

The SEM images of the tensile fracture of the Al−Cu cable joints under the MPC process after 20 d of corrosion are shown in Fig. 11. A similar phenomenon to the mentioned fracture morphology of the 10 d corroded Al cable is observed. Snow-

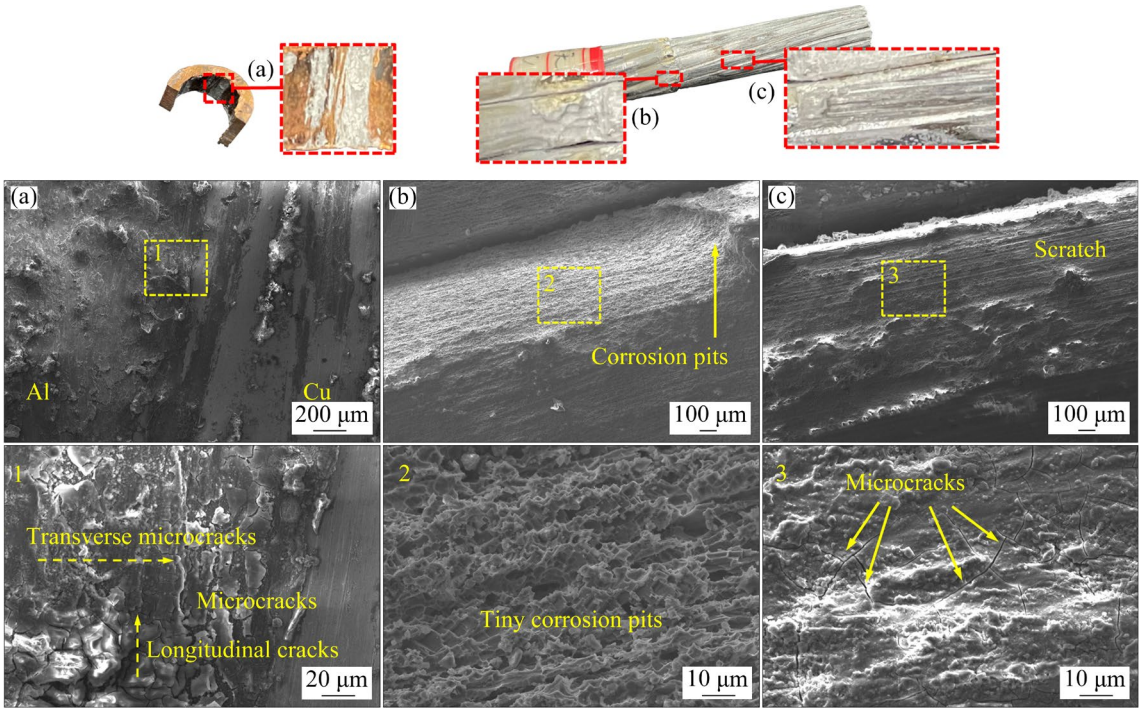

Fig. 9 SEM images of failure surface of Type I joints after 10 d of corrosion: (a) Inner surface of Cu side of lap area; (b) Corrosion pits of Al along edge of lap area; (c) Outer surface of Al side of lap area

like sparse tissue (Area 5), isometric dimples (Areas 1 and 6), shear dimples (Area 7), large cracking phenomena (Areas 2, 3 and 8), numerous corrosion microcracks (Area 9) and stress cracking phenomena (Areas 4, 5 and 8) are found. It is observed that only the fracture of the joint with an

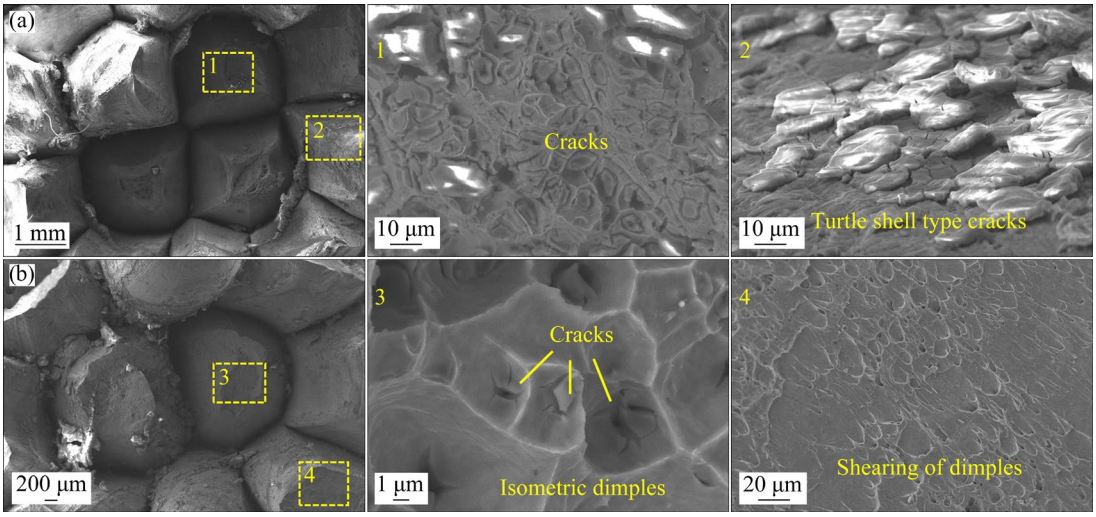

Fig. 10 SEM images of tensile fracture of Al cables in MPC process after 10 d of corrosion: (a) Type II; (b) Type III

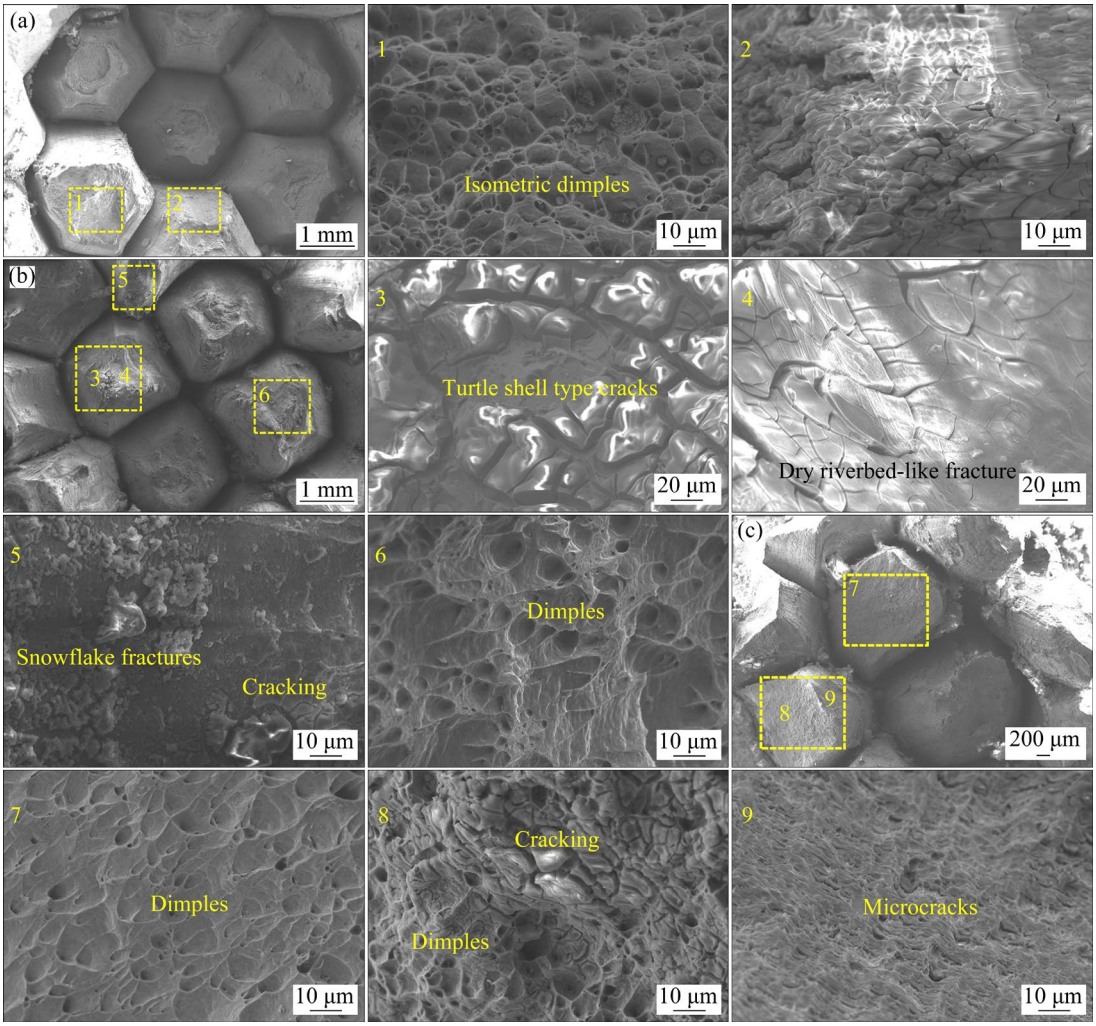

Fig. 11 SEM images of tensile fracture of Al cables in MPW process after 20 d of corrosion: (a) Type I; (b) Type II; (c) Type III

air gap of 2.0 mm exhibits shear dimples, as shown in Area 6 in Fig. 9(b) and Area 7 in Fig. 11(c). As corrosion continues, the shear dimples are transferred from the outer to the inner. Besides, the phenomenon is correlated with the degree of corrosion and force state of the joint. The corrosion pits of the Al cable are larger degree of corrosion, which leads to a greater degree of one-sided tilting of the joint occurring during the tensile process. The change in the proportional distribution of the positive and tangential stresses to which part of the core causes the shear dimples to move inward.

The SEM images of the tensile fracture of the Al cable of the MPC joints after 40 d of corrosion are given in Fig. 12. The degree of corrosion of the Al in the joint is great at this state. Some of the Al cables in the Type III joints have even failed by natural corrosion fracture. It is evident from Fig. 12(a) that little signs of ductile fracture (i.e., the presence of dimples) are still present in the fracture of the Type I joint. Large pieces of cracking as well as stress corrosion cracking are observed in both the frontal and lateral fractures of the Al (Areas 1, 2 and 3). The size of the equiaxial and shear dimples in the transient fracture zone tends to decrease gradually with increasing corrosion cycles according to Figs. 10−12. Moreover, increasingly severe cracking is observed: the cracks grow and the corrosion pits become more widespread and extensive. The reason for this is the presence of residual stress inside the joints after corrosion. When the cable breaks in tension, cracks appear under the combined action of tensile and residual stresses. The longer the corrosion cycle is, the greater the residual stresses generate inside the cable, which leads to faster and severer crack expansion after stretching.

Peeling is highly likely to occur during corrosion due to the aluminum cable being squeezed during the joining process, so that the cable texture is elongated [32−35]. The evolution of the law of pitting corrosion → intergranular corrosion → peeling thus leads to snow-like corrosion material, peeling, chalking and other phenomena. Both the intensification of cable spalling and the accumulation of residual stress can significantly affect the performance of the cable joints. Additionally, a gradual increase in reflective bright white areas is also observed. This may be the corrosion process to generate non-conductive Al oxide, Al hydroxide, sodium meta-aluminate, sodium feldspar and other corrosion products.

The corrosion performance of the joint is also affected by the air gap. Better sealing of the joint can be achieved when the air gap increases. However, the severe extrusion of the aluminum cable leads to severe grain deformation. The grain elongation is more vulnerable to the influence of external thrust from corrosion products. This leads to the appearance of severer pitting, cracking, and laminar corrosion.

The corrosion state of Cu terminals also affects the joint performance. Hence, the microscopic corrosion morphology of the connection end surfaces of the Cu terminals was observed by SEM (see Fig. 13). It can be seen that the Cu terminal end

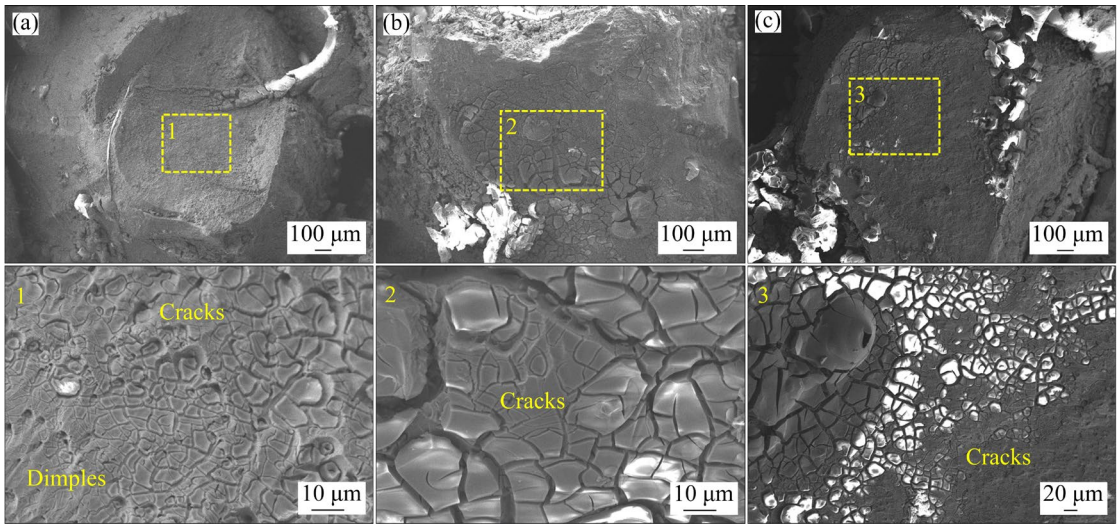

Fig. 12 SEM images of tensile fracture of Al cables in MPW process after 40 d of corrosion: (a) Type I; (b) Type II; (c) Type III

face appears as deformation lines obviously. These are the wrinkles produced by extrusion and shrinkage. Furthermore, a large number of micro-cracks and pinpoint corrosion products are found on the Cu terminals when Area 1 is observed under high magnification. The corrosion becomes more aggressive as the corrosion cycle increases. Adhesive loose porous corrosion products (Area 2) and separated loose porous corrosion products (Area 3) are found. It indicates that the end face of the Cu terminal is not completely cathodic protected by the Al cable. This may have some effect on the electrical performance of the cable joints.

The corroded Al cable was analyzed by EDS surface scan to further study the corrosion products and element distribution during the corrosion process. The results are illustrated in Fig. 14. The EDS elemental analysis shows the presence of elemental chlorine on all corroded surfaces, which implies the formation of $AlCl_3$ after corrosion. The atomic distribution of the elements shows that Al has the highest atomic content, followed by O. This is due to the oxidation and corrosion of Al wire in the salt spray environment to produce $Al(OH)_3$ and Al_2O_3. However, the results show that the proportion of Al atoms increases and the proportion of oxygen elements decreases as the corrosion cycle increases. This is mainly due to the more serious corrosion of Al cable, resulting in the surface of the cable peeling, and chalking phenomenon. As these corrosion products are loosely attached to the cable surface, ultrasonic cleaning easily removes them. Thus, the fresh pure aluminum inside is exposed. This is confirmed by the deepening of the green color in Fig. 14.

The fracture morphology of the Al cable after tensile failure is presented in Fig. 14(d). It can be found that the bright white corrosion product of the fracture is mainly $Al(OH)_3$ according to the elemental atomic content. Al cable experiences stress corrosion cracking during breakage, with large amount of chloride ions adsorbed on the surface and in the cracks. In addition, fracturing and cracking occur under internal stresses during pull-off and stripping. Corrosion products become fragmented and fluffy.

The surface morphology of the corrosion pits at the junction and free ends was observed by SEM in order to compare and analyze the effects of stress corrosion and galvanic corrosion on the cable. The Type II joints with 10 and 40 d of corrosion were selected for observation. Figures 15(a, b) illustrate the corrosion pits. Figures 15(c, d) show the free end morphology. First of all, it is obvious that no matter which position, the corrosion cycle increases with the corrosion degree more and more obvious. Comparison of the corrosion at different locations reveals that the corrosion at the junction of corrosion pits is much greater than the surface of the free end of the Al cable under the action of galvanic corrosion. Moreover, it is found that under galvanic corrosion more regular microcracks and dense tiny corrosion pits appear. Instead, the free end of Al exhibits spalling and irregular cracks on the surface as illustrated in Area 1 due to the stress corrosion effect.

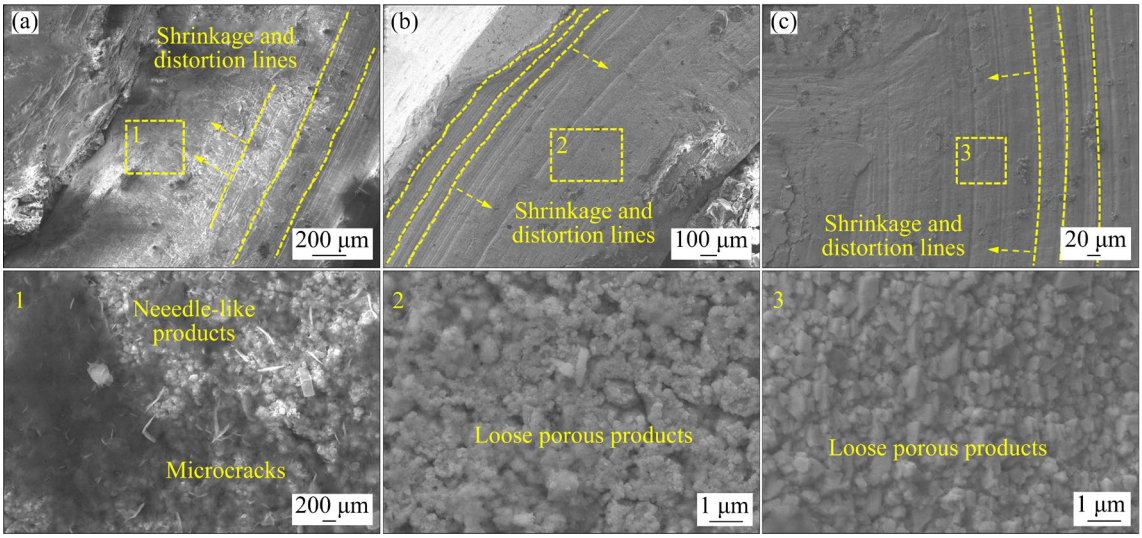

Fig. 13 SEM images of Cu terminals along edge of lap zone of Al−Cu joints at different corrosion cycles: (a) 10 d (Type III); (b) 20 d (Type II); (c) 40 d (Type II)

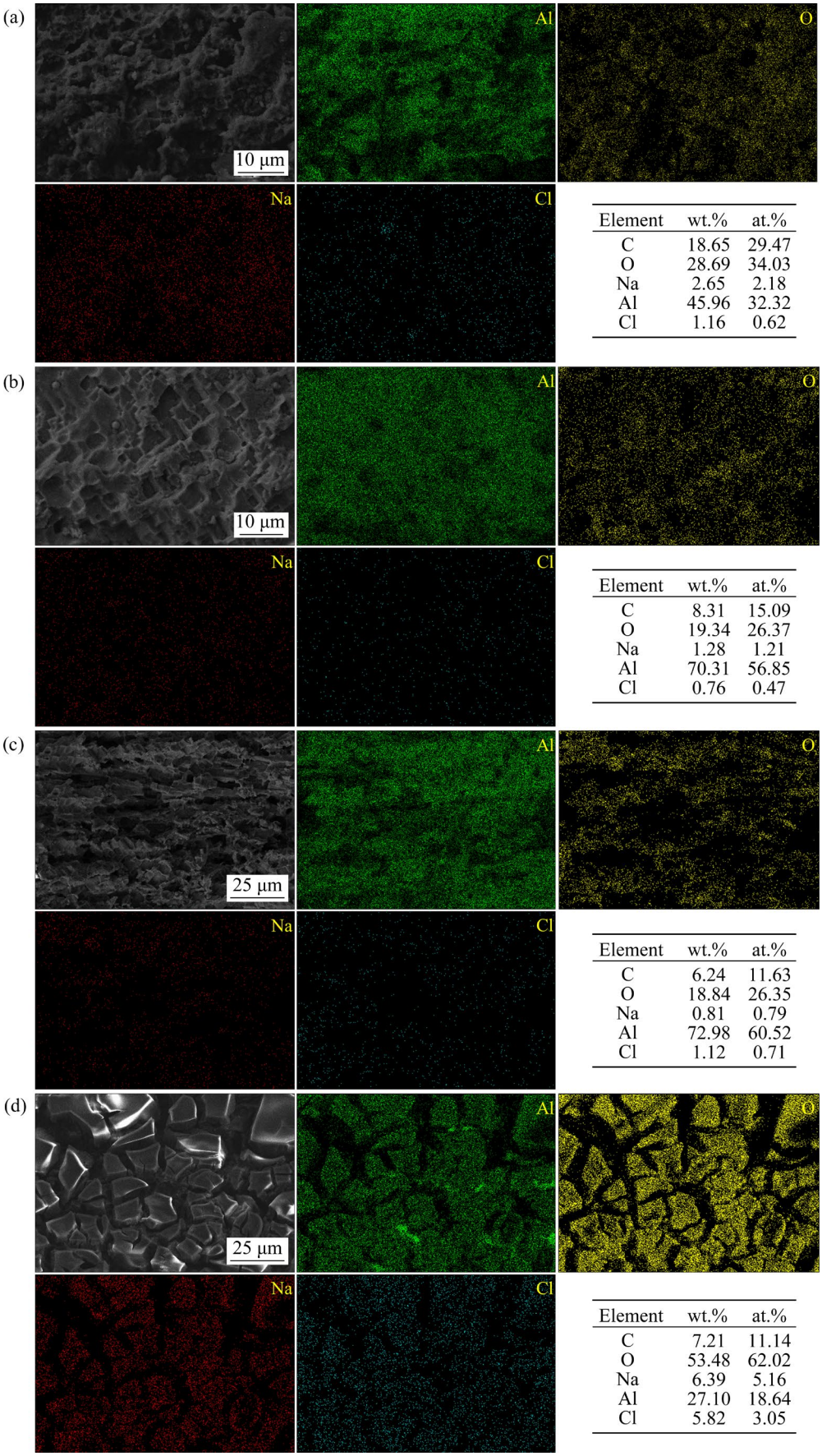

Element	wt.%	at.%
C	18.65	29.47
O	28.69	34.03
Na	2.65	2.18
Al	45.96	32.32
Cl	1.16	0.62

Element	wt.%	at.%
C	8.31	15.09
O	19.34	26.37
Na	1.28	1.21
Al	70.31	56.85
Cl	0.76	0.47

Element	wt.%	at.%
C	6.24	11.63
O	18.84	26.35
Na	0.81	0.79
Al	72.98	60.52
Cl	1.12	0.71

Element	wt.%	at.%
C	7.21	11.14
O	53.48	62.02
Na	6.39	5.16
Al	27.10	18.64
Cl	5.82	3.05

Fig. 14 EDS scan results of corrosion pits and fractures in Al cable: (a) Type I, 10 d; (b) Type II, 20 d; (c) Type II, 40 d; (d) Type III, 40 d

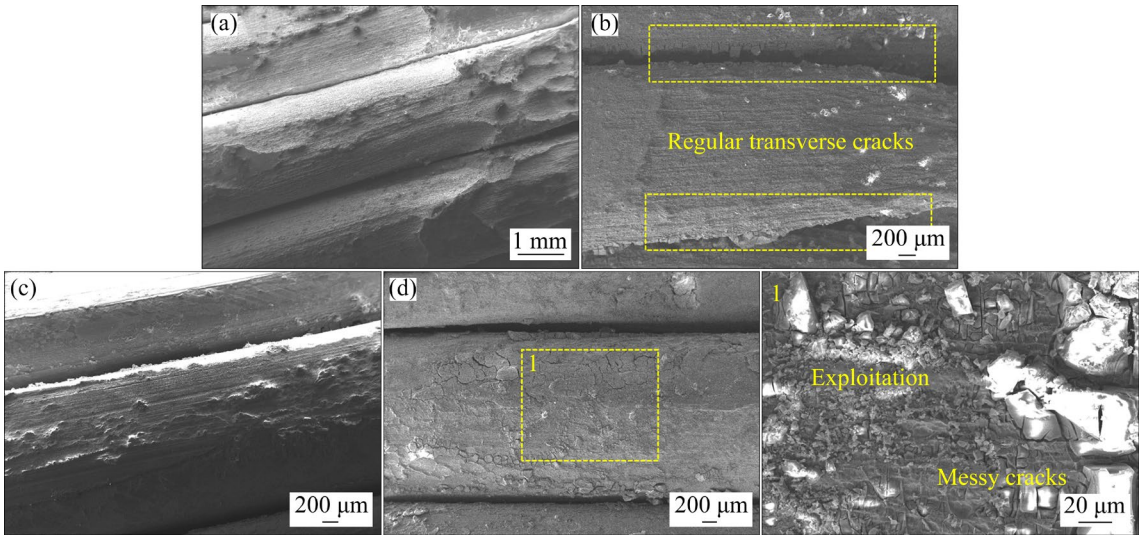

Fig. 15 SEM images of different locations of Al cable after corrosion: (a, b) Corrosion pits at junction; (c, d) Free end surface

3.6 Corrosion mechanism

A comprehensive analysis of the above can summarize the corrosion and failure mechanism of Al−Cu cable joints under a neutral salt spray environment, as shown in Fig. 16. The initial state of the cable joint without corrosion is illustrated in Fig. 16(a). The corrosion process actually has several parts suffering from erosion: Al cable exposed area, Cu terminal exposed area and Al−Cu lap area. All three areas are subjected to the erosive effect of salt spray and produce the corresponding oxides. CuO (black), Cu_2O (brick-red), $Cu_2(OH)_2CO_2$ and $Cu_2(OH)_3Cl$ (green) are generated on the Cu exposed area of the Cu terminal after corrosion. The change process is shown in Fig. 16(d). However, there is no obvious corrosion mark, only tiny corrosion pits appear, as shown in Fig. 16(d′).

In contrast, Al cables exhibit relatively severe corrosion when exposed. There are two main reasons. First, the wire material is pure Al, which is not inherently resistant to corrosion. Furthermore, the salt spray easily invades when the corrosion cycle is extended to destroy the protective role of the Al oxide layer for further corrosion. The corrosion process is illustrated in Fig. 16(b). Second, the salt spray pool of water drips will flow down from the free end of the cable due to the low location. It causes the accumulation of a large number of corrosion products at its end, which will be destroyed after a certain amount of buildup, thus generating large residual stress inside the Al. Hence, a large number of smaller corrosion pits and cracks appear on Al due to stress corrosion, as illustrated in Fig. 16(b′).

The corrosion process of the lap area is shown in Fig. 16(c). The overlap area is mainly subjected to galvanic corrosion. Additionally, the hydrolysis reaction and stripping phenomenon accelerate the corrosion of Al cable to promote the formation of corrosion pits. Hence, the corrosion process consists of two main parts. The first part is in the early stages of corrosion, and a dense oxide layer is formed on the surface of the Al cable near the lap zone. When corrosion further continues, the salt spray will adhere to the cable and collect as droplets due to the difficulty of salt spray entering the well-sealed joint. Al dissolves into Al^{3+} under the action of Cl^-. Moreover, the accumulation of Al^{3+} attracts the external Cl^- to migrate inwards, and the Al^{3+} undergoes a hydrolysis reaction to form $Al(OH)_3$ at the later stage. At the same time, the hydrolysis reaction leads to acidification in the vicinity of the lap area, which further promotes the dissolution of Al. This corrosion phenomenon continues to lead to a deepening of the corrosion pit and finally the Al wire fractures. The second part is the galvanic corrosion of the Al−Cu primary battery. Since Al has a low corrosion potential, the anode loses electrons and Al is dissolved in the cell while Cu is protected from electrons. These two corrosion effects simultaneously promote the formation of deep corrosion pits, as depicted in Fig. 16(c′).

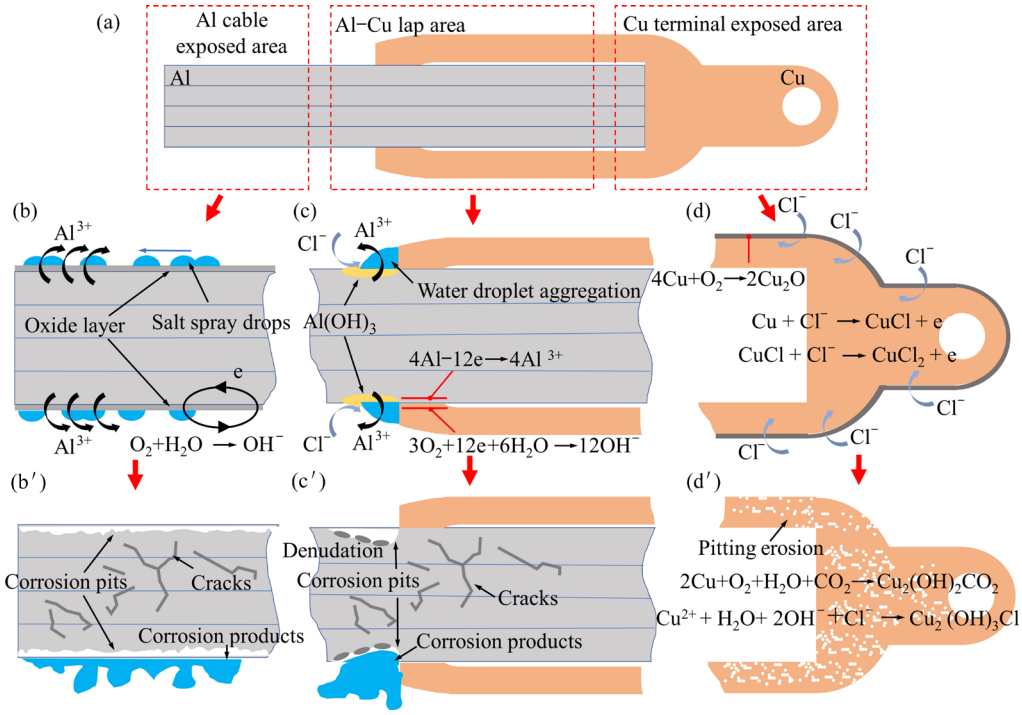

Fig. 16 Corrosion process diagram of cable joint: (a) Initial state without corrosion; (b, b′) Corrosion process of Al cable away from lap zone; (c, c′) Corrosion process of Al cable in lap zone; (d, d′) Corrosion process of Cu terminal away from lap zone

4 Conclusions

(1) The EDS results show that the main products of Al cable corrosion are $Al(OH)_3$ and Al_2O_3. Cu terminal surface pitting corrosion products are Cu_2O, CuO, $Cu_2(OH)_2CO_2$ and $Cu_2(OH)_3Cl$. Furthermore, electrochemical test results demonstrate that MPC joints offer superior corrosion resistance compared with HCC joints.

(2) The accumulation of corrosion products within the joint increases internal tensile friction. This results in an increase in the tensile strength of Type IV joints. However, this buildup also causes a sharp rise in the contact resistance of the cable joint, which increases from 97.2 to 1316.5 μΩ.

(3) The life trend indicates that during the first 20 d of corrosion, the depth of the corrosion pits in Type II joints increases rapidly to 1400 μm and stabilizes between 20 and 40 d, slowly increasing to 1600 μm. In contrast, the depth of the corrosion pits in Type IV joints increases linearly.

(4) The analysis of corrosion products and the stripping mechanism reveals that the joints are primarily subjected to a combination of stress corrosion and galvanic corrosion, which together contribute to cracking and stripping phenomena.

CRediT authorship contribution statement

Yuan-heng YAO: Conceptualization, Methodology, Investigation, Validation, Writing − Original draft, Writing − Review & editing, Visualization; **Shao-luo WANG:** Conceptualization, Methodology, Investigation, Formal analysis, Validation, Writing − Original draft, Writing − Review & editing, Funding acquisition; **Hao JIANG:** Conceptualization, Methodology, Investigation, Formal analysis, Funding acquisition, Validation, Writing & editing; **Jun-jia CUI:** Conceptualization, Data curation, Formal analysis, Funding acquisition, Supervision, Resources, Writing − Review & editing; **Guang-yao LI:** Funding acquisition, Supervision, Resources, Project administration; **Kai-dong LUO** and **Ling-hua XIA:** Conceptualization, Methodology, Validation, Writing & editing.

Declaration of competing interest

The authors declare that they have no known competing financial interests or personal relationships that could have appeared to influence the work reported in this paper.

Acknowledgments

This work is supported by the National Natural Science Foundation of China (No. 52175315), the Shenzhen Science and Technology Program, China (No. KQTD20200820113110016), and the Hunan

Provincial Postgraduate Research Innovation Program, China (No. CX20220404).

References

[1] LI Qing-ya, TIAN Yu-hang, WU Di, GAO Wei, YU Yu-guo, CHEN Xiao-jun, YANG Cheng-wei. The nonlinear dynamic buckling behaviour of imperfect solar cells subjected to impact load [J]. Thin-Walled Structures, 2021, 169: 108317. https://doi.org/10.1016/j.tws.2021.108317.

[2] WAN D, HAGEN A B, VIESPOLI L M, JOHANSON A, BERTO F, ALVARO A. In-situ tensile and fatigue behavior of electrical grade Cu alloy for subsea cables [J]. Materials Science and Engineering: A, 2022, 835: 142654. https://doi.org/10.1016/j.msea.2022.142654.

[3] LU He-wan, YE Fu-xing, WANG Yong-hui. Orthogonal experiments and bonding analysis of ultrasonic welded multi-strand single core copper cables [J]. Journal of Manufacturing Processes, 2022, 78: 1−10. https://doi.org/10.1016/j.jmapro.2022.04.007.

[4] CHENG Xian-ming, YANG Ke, LIU Si-zhan, JI Shan-lin, WANG Jian. Microstructure and mechanical properties of ultrasonic welded copper to aluminum cables joints [J]. Transactions of Nonferrous Metals Society of China, 2023, 33: 3027−3038. https://doi.org/10.1016/S1003-6326(23)66315-0.

[5] YOU Jia-qing, ZHAO Yun-qiang, DONG Chun-lin, SU Yun-hai. Improving the microstructure and mechanical properties of Al−Cu dissimilar joints by ultrasonic dynamic-stationary shoulder friction stir welding [J]. Journal of Materials Processing Technology, 2023, 311: 117812. https://doi.org/10.1016/j.jmatprotec.2022.117812.

[6] MAO Yue, QIN Ding-qiang, XIAO Xuan, WANG Xin-cheng, FU Li. Achievement of high-strength Al/Cu dissimilar joint during submerged friction stir welding and its regulation mechanism of intermetallic compounds layer [J]. Materials Science and Engineering: A, 2023, 865: 144164. https://doi.org/10.1016/j.msea.2022.144164.

[7] MA Qiu-chen, SONG Cheng, ZHOU Jian-li, ZHANG Lin, JI Hong-jun. Dynamic Weld evolution during ultrasonic welding of Cu−Al joints [J]. Materials Science and Engineering: A, 2021, 823: 141724. https://doi.org/10.1016/j.msea.2021.141724.

[8] HUO Peng-da, LI Feng, WANG Ye, LI Chao. Corrugated interface structure and formation mechanism of Al/Mg/Al laminate rolled by hard plate [J]. Transactions of Nonferrous Metals Society of China, 2023, 33: 1038−1053. https://doi.org/10.1016/S1003-6326(23)66164-3.

[9] WANG Jian, WANG Xiao-wei, LI Bo, CHEN Cheng, LU Xiao-feng. Interface repairing for AA5083/T2 copper explosive composite plate by friction stir processing [J]. Transactions of Nonferrous Metals Society of China, 2021, 31: 2585−2596. https://doi.org/10.1016/S1003-6326(21)65677-7.

[10] GHARAHSHIRAN M R K, KHOSHAKHLAGH A, KHALAJ G, BAKHTIARI H, BANIHASHEMI A R. Effect of postweld heat treatment on interface microstructure and metallurgical properties of explosively welded bronze−carbon steel [J]. Journal of Central South University, 2018, 25: 1849−1861. https://doi.org/10.1007/s11771-018-3874-9

[11] JACHSO R L. Electrical performance of aluminium/copper bolted joints [J]. IEE Proceedings C (generation, transmission and distribution). 1982, 129: 177−184.

[12] YAO Yuan-heng, JING Li-jun, WANG Shao-luo, LI Guang-yao, CUI Jun-jia, TANG Xiao-han, JIANG Hao. Mechanical properties and joining mechanisms of Al−Fe magnetic pulse welding by spot form for automotive application [J]. Journal of Manufacturing Processes, 2022, 76: 504−517. https://doi.org/10.1016/j.jmapro.2022.02.017.

[13] SOFI K, HAMZAOUI M, IDRISSI H E, MOH A N S, JOUAFFRE D, HAMZAOUI A. Electromagnetic pulse generator: An analytical and numerical study of the Lorentz force in tube crimping processes [J]. CIRP Journal of Manufacturing Science and Technology, 2020, 31: 108−118. https://doi.org/10.1016/j.cirpj.2020.10.002.

[14] KHALAJ G, MORADI M, ASADIAN E. Exploring the impact of rolling temperature on interface microstructure and mechanical properties of steel–bronze explosive welded bilayer composite sheets [J]. Welding in the World, 2023, 67: 1411−1425. https://doi.org/10.1007/s40194-023-01495-6.

[15] KUMAR R, KORE S D. Effects of surface profiles on the joint formation during magnetic pulse crimping in tube-to-rod configuration [J]. International Journal of Precision Engineering and Manufacturing, 2017, 18: 1181−1188. https://doi.org/10.1007/s12541-017-0138-9.

[16] WEDDELING C, WALTER V, HAUPT P, TEKKAYA A E, SCHULZE V, WEIDENMANN K A. Joining zone design for electromagnetically crimped connections [J]. Journal of Materials Processing Technology, 2015, 225: 240−261. http://dx.doi.org/10.1016/j.jmatprotec.2015.06.009.

[17] LAI Ming, LIU Xiao, WANG Shao-luo, JIANG Hao, LI Guang-yao, CUI Jun-jia. Realizing quality inspection in magnetic pulse crimping manufacturing: Using Steger algorithm and self-attention [J]. Journal of Materials Processing Technology, 2023, 311: 117799. https://doi.org/10.1016/j.jmatprotec.2022.117799.

[18] KUMAR D, KORE S D, NANDY A. Experimental investigation of Cu−SS electromagnetically assisted adhesive tube-to-tube joining: Its advantages over electromagnetic crimping [J]. International Journal of Adhesion and Adhesives, 2021, 109: 102908. https://doi.org/10.1016/j.ijadhadh.2021.102908.

[19] RAJAK A K, KORE S D. Experimental investigation of aluminium−copper wire crimping with electromagnetic process: Its advantages over conventional process [J]. Journal of Manufacturing Processes, 2017, 26: 57−66. https://doi.org/10.1016/j.jmapro.2017.01.009.

[20] KUMAR D, MURTHY K, KORE S D, NANDY A. Effect of thread angle besides other process parameters in electromagnetically crimped threaded surfaced tube-to-tube joint: FEM modelling and ANOVA analysis [J]. Materials Today Proceedings, 2023: 16. https://doi.org/10.1016/j.matpr.2023.02.074.

[21] GUO Fu-qiang, DUAN Shu-wei, PAN Yu-zhe, WU Dong-ting, MATSUDA K, WANG Tao, ZOU Yong. Stress corrosion behavior and microstructure analysis of Al−Zn−Mg−Cu alloys friction stir welded joints under different aging conditions [J]. Corrosion Science, 2023, 210: 110821. https://doi.org/10.1016/j.corsci.2022.110821.

[22] ZHANG D, JIANG H C, CUI Z J, YAN D S, SONG Y Y, RONG L J. Synchronous improvement of mechanical properties and stress corrosion resistance by stress-aging coupled with natural aging pre-treatment in an Al−Zn−Mg

alloy with high recrystallization fraction [J]. Journal of Materials Science & Technology, 2022, 121: 40−51. https://doi.org/10.1016/j.jmst.2021.11.068.
[23] DING Sheng-li, ZHOU Meng-cheng, LIU Xue-bing, LIU Chang-hao, ZHANG Xin-fang. Improving the stress corrosion cracking resistance of aged SA508-309L dissimilar metal weld joints by pulsed electric current [J]. Materials Science and Engineering: A, 2022, 849: 143506. https://doi.org/10.1016/j.msea.2022.143506.
[24] YE Zheng, HUANG Ji-hua, YANG Hao, LIU Tao, YANG Jian, CHEN Shu-hai. Effect of Si addition on corrosion behaviors of Cu/Al dissimilar joint brazed with novel Zn−Al−*x*Si filler metals [J]. Journal of Materials Research and Technology, 2019, 8: 5171−5179. https://doi.org/10.1016/j.jmrt.2019.08.040.
[25] JANDAGHI M R, SABOORI A, KHALAJ G, KHANZADEH G S. Microstructural evolutions and its impact on the corrosion behaviour of explosively welded Al/Cu bimetal [J]. Metals, 2020, 10: 634. https://doi.org/10.3390/met10050634.
[26] SAFARALI F S, ABBAS S, ABOLHASSAN N, MOHAMMAD K G, GHOLAMREZA K. Investigating the effect of post weld heat treatment on corrosion properties of explosive bonded interface of AA5083/AA1050/SS 321 tubes [J]. Materials Research Express, 2020, 7: 036529. https://doi.org/10.1088/2053-1591/ab8095.
[27] OKONKWO B O, MING Hong-liang, WANG Jian-qiu, HAN E H, RAHIMI E, DAVOODI A, HOSSEINPOUR S. A new method to determine the synergistic effects of area ratio and microstructure on the galvanic corrosion of LAS A508/309 L/308 L SS dissimilar metals weld [J]. Journal of Materials Science & Technology, 2021, 78: 38−50. https://doi.org/10.1016/j.jmst.2020.10.044.
[28] HUANG Shi-yu, LIU Heng, SU Yan-jing, QIAO Li-jie, YAN Yu. Significant influence of trace Li on the mechanical properties, corrosion behavior, and antibacterial properties of biodegradable Zn−4Cu alloys [J]. Journal of Materials Science & Technology, 2023, 151: 245−257. https://doi.org/10.1016/j.jmst.2022.12.045.
[29] WANG Shao-luo, LUO Kang, SUN Tao, LI Guang-yao, CUI Jun-jia. Corrosion behavior and failure mechanism of electromagnetic pulse welded joints between galvanized steel and aluminum alloy sheets [J]. Journal of Manufacturing Processes, 2021, 64: 937−947. https://doi.org/10.1016/j.jmapro.2021.02.039.
[30] GENG Hui-hui, CUI Jun-jia, LI Guang-yao, MAO Jing-qi, YE Liang. Mechanical degradation of magnetic pulse welded Al−Fe joint in neutral salt environment [J]. Journal of Materials Research and Technology, 2021, 15: 2365−2378. https://doi.org/10.1016/j.jmrt.2021.09.078.
[31] ZHANG Peng, ZHU Qiang, SU Qian, GUO Bin, CHENG Shu-kang. Corrosion behavior of T2 copper in 3.5% sodium chloride solution treated by rotating electromagnetic field [J]. Transactions of Nonferrous Metals Society of China, 2016, 26: 1439−1446.
[32] ROBINSON M J. The role of wedging stresses in the exfoliation corrosion of high strength aluminium alloys [J]. Corrosion Science, 1983, 23: 887−899. https://doi.org/10.1016/0010-938X(83)90016-1.
[33] WANG Li-wei, LIANG Jian-ming, LI Han, CHENG Lian-jun, CUI Zhong-yu. Quantitative study of the corrosion evolution and stress corrosion cracking of high strength aluminum alloys in solution and thin electrolyte layer containing Cl^- [J]. Corrosion Science, 2021, 178: 109076. https://doi.org/10.1016/j.corsci.2020.109076.
[34] MA Zhi-min, LIU Jia, YANG Zhen-shen, LIU Sheng-dan, ZHANG Yong. Effect of cooling rate and grain structure on the exfoliation corrosion susceptibility of AA 7136 alloy [J]. Materials Characterization, 2020, 168: 110533. https://doi.org/10.1016/j.matchar.2020.110533.
[35] ROBINSON M J. Mathematical modelling of exfoliation corrosion in high strength aluminium alloys [J]. Corrosion Science, 1982, 22: 775−790. https://doi.org/10.1016/0010-938X(82)90013-0.

采用磁脉冲压接的铝铜电缆接头在盐雾环境中的腐蚀行为和性能退化

姚源恒[1]，王绍螺[1]，蒋 浩[1]，崔俊佳[1,2]，李光耀[1,2]，罗开东[3]，夏铃华[3]

1. 湖南大学 整车先进设计制造技术全国重点实验室，长沙 410082；
2. 北京理工大学 深圳汽车研究院，深圳 518118；
3. 弗迪电池有限公司 第一生产部，惠州 516083

摘 要：比较铝电缆和铜端子接头在磁脉冲压接(MPC)和液压钳压接(HCC)条件下的耐腐蚀性能。通过力学和电学性能评估性能退化的情况。此外，通过电化学测试分析接头的腐蚀行为。使用扫描电子显微镜(SEM)和能量色散光谱(EDS)对其进行微观表征。结果表明，腐蚀接头的抗拉强度降低。然而，由于 MPC 独有的高速成形和接触紧密性优势，腐蚀接头的接触电阻仍然保持良好。电化学测试表明，MPC 接头具有更高的腐蚀电位和更小的腐蚀电流，表现出更好的耐腐蚀性。铝和铜在搭接处形成了原电池，导致形成更严重的腐蚀坑。

关键词：磁脉冲压接；铝铜电缆接头；盐雾腐蚀；性能退化；腐蚀机理

(Edited by Xiang-qun LI)